Tunable Nanoparticle Arrays at Charged Interfaces

Sunita Srivastava,[†] Dmytro Nykypanchuk,[†] Masafumi Fukuto,[‡] and Oleg Gang*[,†]

[†]Center for Functional Nanomaterials, Brookhaven National Laboratory, Upton, New York 11973, United States, and [‡]Condensed Matter Physics and Materials Science Department and Photon Sciences Directorate, Brookhaven National Laboratory, Upton, New York 11973, United States

ABSTRACT Structurally tunable two-dimensional (2D) arrays of nanoscale objects are important for modulating functional responses of thin films. We demonstrate that such tunable and ordered nanoparticles (NP) arrays can be assembled at charged air-water interfaces from nanoparticles coated with polyelectrolyte chains, DNA. The electrostatic attraction between the negatively charged nonhybridizing DNA-coated gold NPs and a positively charged lipid layer at the interface facilitates the formation of a 2D hexagonally closed packed (HCP) nanoparticle lattice. We observed about 4-fold change of the monolayer nanoparticle density by varying the ionic strength of the subphase. The tunable NP arrays retain their structure reasonably well when transferred to a solid support. The influence of particle's DNA corona and lipid layer composition on the salt-induced in-plane and normal structural evolution of NP arrays was studied in detail using a combination of synchrotron-based *in situ* surface scattering methods, grazing incidence X-ray scattering (GISAXS), and X-ray reflectivity (XRR). Comparative analysis of the interparticle distances as a function of ionic strength reveals the difference between the studied 2D nanoparticle arrays and analogous bulk polyelectrolyte star polymers systems, typically described by Daoud—Cotton model and power law scaling. The observed behavior of the 2D nanoparticle array manifests a nonuniform deformation of the nanoparticle DNA corona due to its electrostatically induced confinement at the lipid interface. The present study provides insight on the interfacial properties of the NPs coated with charged soft shells.

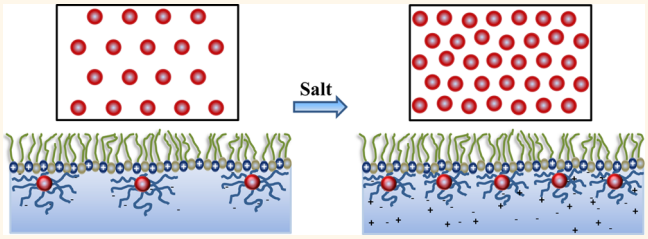

KEYWORDS: self-assembly · lipid membrane · liquid interfaces · charged nanoparticle

A structural organization of nanoparticles (NP) into two-dimensional (2D) arrays with tunable interparticle distances is of importance for fabrication of photovoltaic devices,[1,2] metamaterials,[3] optically tailored coatings,[4−6] and magnetic storage media.[7,8] From a fundamental perspective, there is a broader interest to understand the key physical parameters influencing assembly of nanoscale objects, which often includes inorganic core and soft organic shell, in reduced dimensions and their interactions with the environment. The interfacial interactions between the polymeric and the inorganic components under confinement can alter the structure as well as macroscopic behavior of the assembly in a complex manner.[9−12] The construction of 2D arrays with conventional methods using spin coating,[13] drying mediated deposition of NPs on solid surfaces,[14] allows for fabrication of static arrays. Alternatively, assembly of nanoobjects at liquid interfaces, for example, by using Langmuir monolayers of charged lipids was shown to yield 2D assemblies with controlled surface density.[15] The lipid monolayer facilitates the adsorption of nanoparticles at the liquid—air interface through electrostatic interaction *via* the counterion release mechanism,[10,16] while at the same time intrinsic fluidity of the interface allows for particle mobility, which is important for nanoparticle rearrangement and for a long-range order.[17−19]

Besides the fundamental and technological aspects of NP self-assembly at the lipid interface, there is a growing interest in understanding the interactions of nanoparticles with lipid membranes.[20−22] This is due to the analogy of synthetic NP with naturally occurring macromolecular constructs, and emerging questions in nanotoxicology and nanomedicine. For instance, the lipid—nanoparticle hybrids can be exploited to encapsulate drugs in lipid vesicles for targeted delivery,[23,24] while the nanoparticle acts as a functional probe[25] providing contrast for imaging or response in any external simulation, *e.g.* magnetic field.[26] DNA-coated NP was demonstrated as an

* Address correspondence to ogang@bnl.gov.

Received for review July 31, 2014 and accepted September 8, 2014.

Published online September 08, 2014
10.1021/nn5042416

effective platform for gene delivery;[27,28] however, the mechanism of their penetration into a cell is still not well understood. The future biomedical applications of NPs require an understanding of the NP–lipid interactions.

Here we report the salt-controlled behavior of DNA-functionalized gold nanoparticles adsorbed at charged lipid-coated air–water interfaces. Whereas a NP monolayer forms due to attraction between negatively charged DNA shell and positively charged lipid layer, the internal structure of monolayer is determined by interparticle electrostatic repulsions provided by noncomplementary DNA shells. The observed 2D HCP lattice of NPs can be tuned by changing the ionic strength. By studying the evolution of in-plane and surface-normal structure of the NP array, we reveal the role of chain confinement on the interparticle interactions at the interface. We also show that the 2D assembled arrays can be successfully transferred to solid substrates while retaining their order, supporting the potential utility of these structures as a template for 2D patterning.

RESULTS

We investigated the assembly of DNA-coated gold nanoparticles (DNA–NP) on the positively charged lipid layer at the water–air interface. The system consists of NPs of one kind only, with a shell composed of single-stranded (ss) DNAs with nonhybridizing sequences, and therefore, the dominant interactions in the system are electrostatic and steric, and interparticle DNA hybridization can be neglected. We note that use of DNA allows for creation of NP systems with a precisely tailored polyelectrolyte shell: the chains in the shell are monodisperse in size and composition. Thus, the DNA-functionalized NP is an appropriate model system for a quantitative study of the effect of nanoscale interactions at the interface on the structure of NP monolayer.

The schematic of our experimental strategy and the major parameters as defined in the text are shown in Figure 1. The combination of surface-to-particle attraction and interparticle repulsion results in the formation of a highly ordered 2D HCP lattice, as we discuss below. The electrostatic attraction between the cationic lipid layer and the negatively charged single stranded (ss) DNA corona promotes NP adsorption, as shown in the schematic of Figure 1a. A nanoparticle monolayer forms as a result of the balance between the interparticle repulsion due to the same charged DNA shells and the particle-lipid attraction due to the oppositely charged shell and lipid monolayer. We manipulated these interactions by varying the salt concentration by adding NaCl solution in the subphase. The choice of

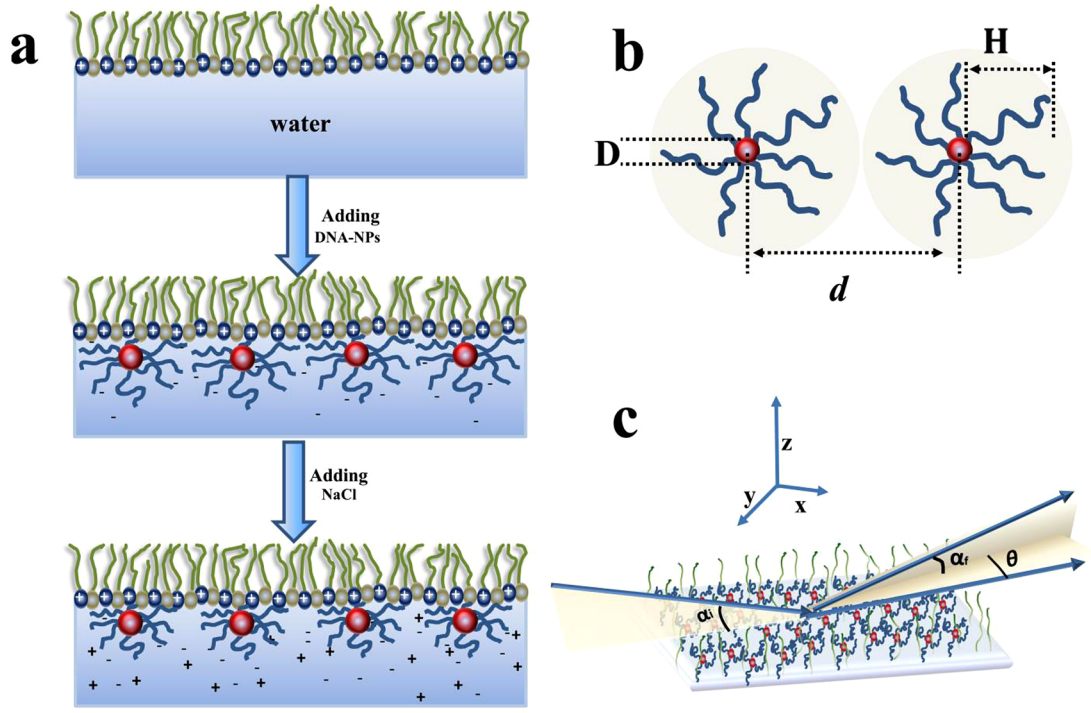

Figure 1. Schematic of the experimental setup. (a) Cross-sectional view of the lipid layer at the air–water interface. On addition of DNA functionalized NPs, the electrostatic interaction results in adsorption and formation of NP monolayer at the interface. With increase in ionic strength by addition of NaCl, the repulsion between DNA chains is screened. (b) The core–corona system used in this study consists of fixed core of size, D = 8.5 nm and corona of thickness H, which was varied between 50 and 65 bases. (c) Schematic for *in situ* surface scattering measurements of 2D assemblies at the air/water interface. An X-ray beam incident on the surface is scattered from the nanocrystalline assemblies and recorded on CCD detector. For XRR, the same setup was used with $\theta = 0^\circ$ and the reflected intensity is recorded on point detector as a function of wave vector.

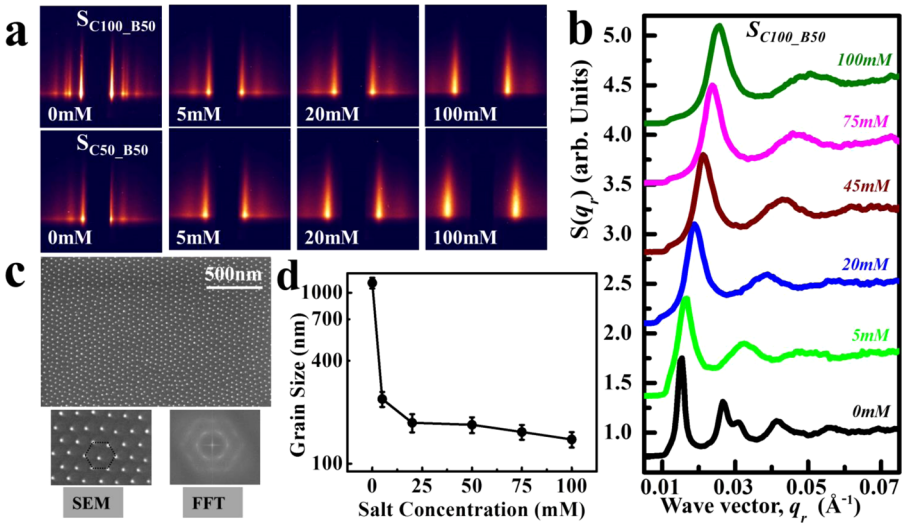

Figure 2. (a) The GISAXS scattering data from 2D assemblies of NPs as a function of salt concentration for S_{C100_B50} (top) and S_{C50_B50} (bottom). (b) The line profiles for S_{C100_B50} at various salt concentrations, indicated alongside each profile. The first diffraction peak position shifts toward higher q_r with increase in salt concentration revealing decrease in in-plane interparticle distance. (c) *Ex situ* SEM image from DNA−NP layer transferred to solid substrate. The high magnification SEM data along with the Fourier transform clearly indicates the formation of HCP lattice. (d) Grain size at different salt concentration for the same system as in (b).

ssDNA is motivated by its polyelectrolyte behavior which permits a broad range of tunability in the interparticle distances with the change in salt concentration.[29] The evolution of the interface-normal and in-plane structure of the monolayer was explored using synchrotron based X-ray reflectivity (XRR) and grazing incidence small-angle X-ray scattering (GISAXS), respectively. The systems of choice include two types of liquid interfaces with different ratios of the neutral lipid 1,2-dimyristoyl-*sn*-glycero-3-phosphocholine (DMPC) and the cationic lipid 1,2-dimyristoyl-3-trimethylammonium-propane (DMTAP), 50/50 and 0/100, respectively, and two types of DNA-coated gold nanoparticles (diameter, $D \sim 8.5 \pm 0.75$ nm) correspondingly functionalized with ssDNA of 50 and 65 bases. This allows probing the effects of both the surface charge and the ssDNA shell on the structure of the 2D assembly. We denote these systems as S_{C50_B50}, S_{C100_B50}, and S_{C100_B65} (the index C designates the content of the cationic lipid, 50% or 100%, and B represents the number of bases in DNA chains). The lipid molecule occupies ~75 Å^2 per headgroup, thus corresponding to one positive charge per 75 Å^2 and per 150 Å^2 for S_{C100} and S_{C50}, respectively.

The GISAXS measurements of the nanoparticle layer reveal the presence of a highly ordered structure (Figure 2). With no added salt (0 mM), the observed GISAXS image displays up to 4-5 Bragg rods that are sharply peaked along the in-plane scattering wave vector, q_r, axis as shown in Figure 2(a) (S_{C100_B50}, S_{C50_B50}) and Figure S2, S3 (S_{C100_B65}). The GISAXS pattern along the q_r direction (at constant $q_z \sim 0.024$ Å^{-1}) is plotted in Figure 2b for system S_{C100_B50}. The estimated peak ratios, $q_i/q_1 \sim 1{:}\sqrt{3}{:}\sqrt{4}{:}\sqrt{7}{:}\sqrt{9}$ (i = 1, 2, 3, ...) satisfies the condition for a HCP lattice. Notably, the obtained GISAXS pattern for the lipid monolayer with only the neutral DMPC lipid shows no evidence of in-plane surface structure or particle adsorption to the interface (Supporting Information Figure S2). This suggests that the positive charge on the lipid layer is essential to promote the 2D assembly through electrostatic attraction. Interestingly, the system with the higher density of cationic lipids exhibits a higher degree of order (S_{C100_B50} *vs* S_{C50_B50}), as indicated by the larger number of observed diffraction peaks and their narrower widths (Figure 2a). Thus, a stronger electrostatic attraction of DNA-NP to the lipid layer results in better 2D order within the NP monolayer. The presence of HCP lattices were also revealed through *ex situ* SEM measurement (Figure 2c) performed on the gold NP monolayer transferred onto a positively charged polymer-coated silicon substrate (see Supporting Information, Figure S4).

The probing of the monolayer structure with increase in salt concentrations shows a decrease in the in-plane interparticle separations and the reduced degree of lattice order, as indicated by the shift in the first diffraction peak to larger q_r and the broadening of the diffraction peaks in the GISAXS data (Figure 2b), respectively. For example, for system S_{C100_B50}, we observed a decrease of grain size, $\xi \sim 2\pi/\Delta q$[30] (where Δq is the resolution-corrected full width of the first diffraction peak) from ~1140 nm at 0 mM to ~140 nm at 100 mM, as shown in Figure 2d, which indicates a significant order decrease within the NP monolayer.

The surface-normal structure of the DNA−NP monolayer at the lipid interface was probed by X-ray reflectivity. The XRR profiles obtained from the bare and DNA−NP (S_{C100_B50}) coated lipid interface at

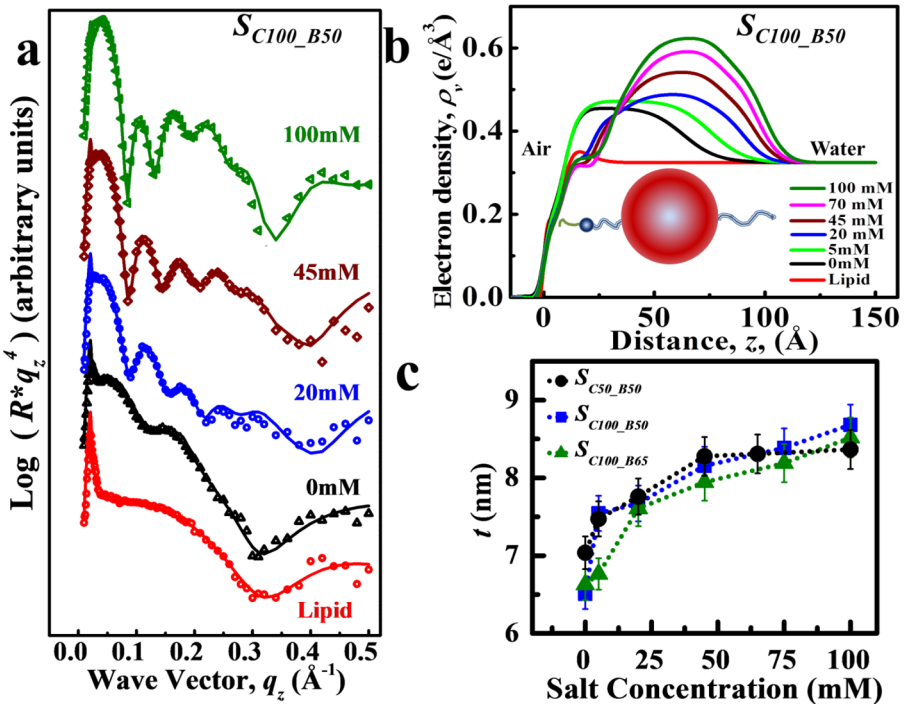

Figure 3. XRR on 2D assembled nanostructures. (a) The XRR data as a function of salt concentration for S_{C100_B50} along with the fit to the data (solid lines) using Moto fit package in IgorPro.[32] The amplitude of oscillation increases and minima of the oscillation shifts toward higher wave vector, with increase in salt concentration. (b) Electron density profile obtained from fit to the data in (a) (cartoon not to scale). (c) Thickness of the DNA−NP layer at the interface obtained by subtracting the thickness of lipid layer from the total layer dimension.

different salt concentrations are shown on a semilog plot as Rq_z^4 where R is the reflectivity signal from a nanoparticle monolayer and q_z is the surface-normal scattering wave vector (Figure 3a). Compared to the XRR profile of the bare lipid interface, the data for the DNA−NP bearing interface show additional modulations at low q_z. The period and amplitude of these modulations are related to the thickness and density of the adsorbed DNA−NP monolayer. A progressive increase in the modulation amplitude and a decrease of the modulation period are observed for all studied systems when the NaCl concentration is increased in steps from 0 to 100 mM, as visible on several representative XRR profiles (Figure 3a). These changes indicate the evolution of the nanoparticle interface toward a denser and thicker DNA−NP layer, as we discuss below.

Detailed quantitative information on the surface-normal structure of the interface was obtained through the fitting of the XRR data using the Parratt algorithm[31,32] (solid lines, Figure 3a, Supporting Information). The obtained electron (*e*) density profiles, ρ_v *vs* z, at different salt concentrations for S_{C100_B50} are plotted in Figure 3b. The maximum value of ρ_v for the lipid monolayer was found to be ~0.35e/Å^3. This value is slightly higher than that of water, ~0.33e/Å^3, and consistent with the lipid headgroup.[33] With the addition of DNA−NP in the subphase and no added salt (0 mM), we observed the formation of an additional layer with high *e*-density just below the lipid, which is attributed to the NP adsorption. Subsequent increase in the salt concentration resulted in gradual increase in the *e*-density and layer thickness. Interestingly, at low salt (≤20 mM), the *e*-density profiles for the NP layer are asymmetric and its maxima are shifted toward the lipid layer. By contrast, a symmetric profile is observed at higher salt concentrations.

The thickness of the DNA−NP layer (Figure 3c), t, was obtained by subtracting the thickness of the lipid layer (~3 nm, as determined from XRR for the initial lipid interface without NP) from the total layer thickness. The DNA−NP layer thickness, t is about 6.5−7 nm with no added salt, and it increases with salt concentration to about 8.7 ± 0.2 nm (S_{C100_B50}), which is close to the diameter of the gold NP core. The evolution of t, together with the asymmetric electron density profile (Figure 3b), suggests that DNA−NPs at low salt concentrations interact strongly with the lipid layer, possibly causing the deformation of the DNA shell, as illustrated in the cartoon in Figure 5b. At the same time, the broader, more symmetric *e*-density distribution observed for the DNA−NP layer at higher salt concentrations reflects a weaker NP−lipid binding. Nevertheless, the increased *e*-density of the NP layer at high salt concentrations indicates that even when highly screened, the electrostatic lipid-DNA attraction is sufficient to drive the DNA−NP adsorption to the interface.

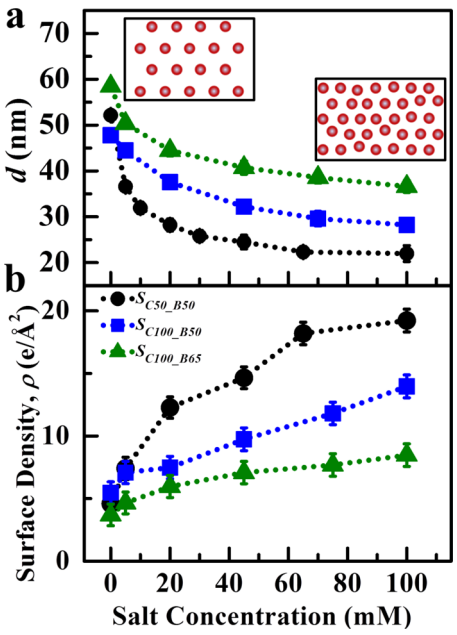

Figure 4. (a) In-plane center−center nanoparticle separation, *d*, as a function of salt concentration for S_{C50_B50} (●), S_{C100_B50} (■), and S_{C100_B65} (▲). Systems S_{C50} and S_{C100} consist of one positive charge per 150 Å^2 and per 75 Å^2, respectively. (b) The estimate of surface density of gold NPs in DNA−NP layer, obtained by integrating the electron density profiles for gold monolayer (refer to text). Symbols are same as (a).

The evolution of GISAXS and XRR-derived measures, interparticle distance *d* and surface density ρ, of the NP array with salt concentration are shown in Figure 4, panels a and b, respectively. The in-plane center-to-center interparticle distances were estimated as, $d = [4\pi/(\sqrt{3}q_{10})]$, where q_{10} is the position of the first diffraction peak in the GISAXS data. For all the studied systems, the in-plane interparticle distance, *d*, monotonically decreases with the salt concentration increase (Figure 4a). The observed by 2-fold *d* change indicates a high degree of tunability of these NP arrays. In Figure 4b, we show the evolution of the excess surface *e*-density ρ, of the gold NPs as a function of a salt concentration, which is calculated by taking the difference between the *z*-integrated *e*-densities for the lipid−subphase interface with and without the adsorbed NP layer. Similar to the reduction in *d* from GISAXS, the surface excess *e*-density, ρ, from XRR was found to increase with salt concentration as shown in Figure 4a,b. We note that at 0 mM salt, the estimated number of excess electrons per area occupied by a single particle ($\sim\rho d^2$) in the NP layer is consistent with the calculated number of excess electrons per gold nanoparticle $\sim [(\rho_V^{Au} - \rho_V^{water}) \times (\pi D^3/6)]$ where *D* denotes the NP core diameter, ρ_V^{Au} and ρ_V^{water} are the bulk *e*-densities of gold and water, respectively. We also note that at any given salt concentration, the comparison between S_{C100_B50} and S_{C100_B65} shows that the longer ssDNA chains result in larger *d* and smaller ρ, as expected.

One of the key results of the present study is the observation that the packing density of the adsorbed DNA−NPs does not scale with the lipid charge density at nonzero salt concentrations. With no added salt, S_{C100_B50}, the system with the higher lipid charge density exhibits both smaller *d* and larger ρ than S_{C50_B50} (Figure 4a,b, 0 mM). Surprisingly, this trend is reversed once salt is added (Figure 4a,b, 5 mM of NaCl and higher). This indicates that interfacial charge has an unusual effect on the morphology of the DNA−NPs within the monolayer in the presence of salt. The possible origin of this complex dependence of *d* and ρ on the lipid layer charge density will be discussed below.

DISCUSSION

The present study demonstrates a directed assembly of ordered 2D arrays of nanoparticles with tunable lattice spacing and packing density. As shown in Figure 4, the nanoparticle packing density can be controlled over a wide range (by a factor of up to 4 or tens of nm in interparticle spacing) simply by varying the salt concentration. The tunability of the interparticle spacing in 2D NP arrays, which has been difficult to achieve with solution-cast[14,34] and Langmuir films,[35−37] is a unique feature of the lipid-supported DNA−NP monolayer.

The remarkable tunability of the 2D nanoparticle density with salt concentration can be qualitatively understood by considering the polyelectrolyte nature of the DNA shell. With added salt, ions in the solution screen the electrostatic repulsion of DNA chains, which results in the reduced persistence length of ssDNA,[29] and accordingly, the DNA shell thickness decreases. The estimate of the Debye screening length at the lowest added salt concentration (5 mM) is ∼4 nm, which is much smaller than the measured interparticle distances for all the systems studied here. The screening of electrostatic repulsion with added salt reduces the range of the electrostatic repulsion between the interface-confined DNA−NPs. These effects should decrease the area occupied by each adsorbed particle at the interface. The newly available free surface area is created, and it allows for adsorbing additional NPs from the subphase. Hence, the 2D nanoparticle density at the interface increases, as confirmed by our XRR measurements (Figure 4b). A concomitant effect of increasing salt concentration is the reduction in in-plane order, as observed by the GISAXS measurements (Figure 2). This result, which likely originates from reduced adsorption of new NPs to the lipid surface at higher salt condition and the weakening of the interparticle repulsive interactions due to the screening, correspondingly highlights the important role of the particle-interface attraction and interparticle repulsion in promoting the in-plane order within NP monolayer. This finding agrees with previous studies that showed

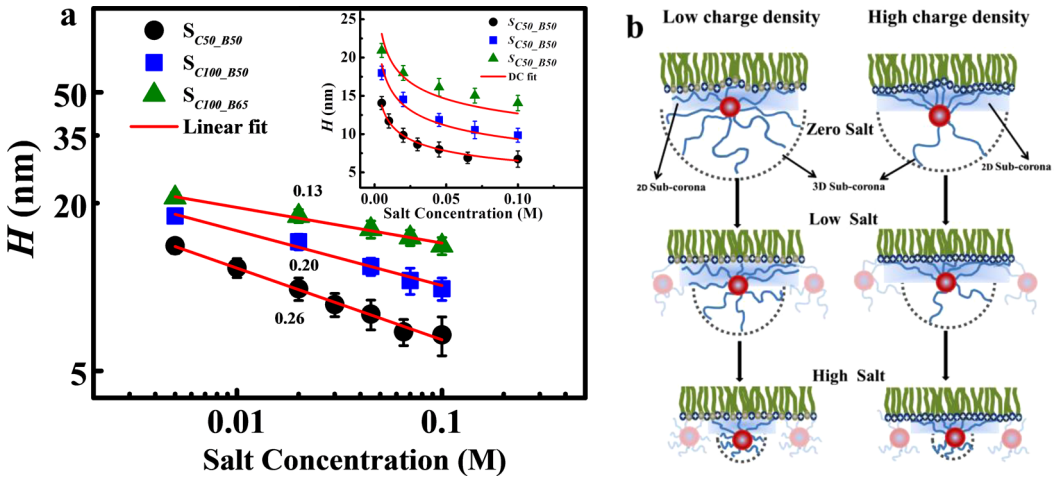

Figure 5. (a) Power law analysis for length of DNA shell, *H vs* C_s (salt concentration) for S_{C50_B50} (●), S_{C100_B50} (■), and S_{C100_B65} (▲). The indicated numbers alongside each data are estimate of power law exponent obtained from linear fit (red solid line). Inset: Analysis using DC model. The red lines are fit to the data (see Supporting Information). (b) Schematic representing the competing role of 2D subcorona and 3D sub corona in defining the in-plane morphology of DNA chains (highlighted nanoparticle) in the NP monolayer, at different strength of DNA−lipid layer interaction. With increase in salt concentration, the dominant shrinkage in 3D subcorona for system with low charge density of lipid layer results in higher exponent as shown in (a). The 2D subcorona is shown by shaded blue color region and the 3D subcorona is marked by dashed circle. The neighboring particles in the 2D HCP lattice at low and high salt are shown with faded color in background around the highlighted nanoparticles.

that repulsive interactions can induce order in 2D arrays of interface-confined particles.[38]

The DNA chain length and the charge density of the lipid layer provide additional control parameters for tuning the 2D packing density of DNA−NPs, as well as for understanding the mechanism of NP array formation and dynamical changes with salt. The ρ dependence on the DNA chain length is in qualitative agreement with the expected behavior. The observation that the in-plane interparticle distance d decreases with the DNA length (S_{C100_B65} *vs* S_{C100_B50}), regardless of the salt concentration, indicates that the 2D packing density depends on the size of the NP-bound DNA corona. In particular, the d-spacings observed for S_{C100_B65} and S_{C100_B50} show that increasing the DNA length by 15 bases results in the increase of the in-plane DNA corona thickness $H = [(d - D)/2]$ (Figure 1b) from 19.7 to 25.0 nm when no salt is added, *i.e.*, for the naturally stretched DNA chains. The relative increase in H by 27% is consistent with the 30% increase in the number of bases per DNA chain.

The intriguing finding of this study is the complex dependence of the 2D packing density of DNA−NPs on the lipid-layer charge density (Figure 4). For the systems with the same DNA length (S_{C50_B50}, and S_{C100_B50}) and no added salt, the higher charge density in the lipid layer leads to a higher NP packing density. This can be explained by the higher affinity of the NPs to the interface with the higher concentration of the cationic lipids. In contrast, in the presence of added salt (5 mM and higher), the system with the lower lipid-layer charge density (S_{C50_B50}, *vs* S_{C100_B50}) is found to exhibit a substantially higher NP packing density. This result implies that the affinity of NP to the interface on its own cannot explain the packing density of NPs at the charged interface, as we have hypothesized above. In the absence of any surface effects, *e.g.*, for 3D superlattices of DNA−NP assembly, the major parameter defining the interparticle distances is the thickness of the DNA shell. However, for the DNA−NP assembly at charged interfaces, the electrostatic interaction of the DNA shells with the lipid layer plays an important role in defining the NP monolayer structure. To explain the observed behavior of d and ρ with salt concentration, we need to consider possible nonuniform changes in the DNA shell structure when the NPs are confined to the interface through electrostatic attraction as discussed below.

To gain insight into the confinement effect on the morphologies of DNA chains at the interface, we compare our data with the scaling prediction of the modified Daoud−Cotton (DC) model for polyelectrolyte brushes (see Supporting Information).[39,40] The model explains well the change in the morphology of charged polymer brushes attached to a curved surface with increase in salt concentration and it can be applied for DNA−NP in solutions due to the morphological similarities of these objects.[41] However, given that the DC is strictly applicable for star polymers in 3D solution, our goal in using this model is to identify the deviation of the observed 2D assembly behavior from the bulk behavior. In the inset of Figure 5 we plot the salt dependence of the in-plane thickness of the DNA shell, H *vs* C_s, where C_s is the salt concentration. The solid lines are fits of the DC model to our experimental data for three different studied systems; thus, the grafting density of DNA chains, Σ, on the nanoparticle surface can be extracted by applying the DC model.

The obtained values of Σ are ~0.1 chains/nm^2 for S_{C50_B50}, 0.5 chains/nm^2 for S_{C100_B50}, and 0.8 chains/nm^2 for S_{C100_B65}, corresponding to the coverage of 23, 113, and 185 chains per/particles, respectively. These values of Σ deviate from the experimentally measured value of 40−60 chains/particle for the DNA−NPs used in this work. This deviation is greater for the systems with the larger lipid charge density and for longer ssDNA chains, being the smallest for S_{C50_B50}, intermediate for S_{C100_B50}, and the largest for S_{C100_B65}. That is, the deviation from the bulk behavior increases with increasing interactions of the DNA−NP monolayer with the charged lipid layer. Interestingly, a recent study on Gibbs monolayers of DNA-coated nanoparticles[34,42] at free air−liquid interfaces found a good agreement with the DC model. We believe that the applicability of the DC model for the Gibbs monolayers was possible due to the nonconfined nature of the DNA−NP layer at the interface, which allowed the DNA chains to retain the bulk confirmation and NP exhibited the solution behavior. In contrast, in the present case the lipid layer causes a strong confinement of the DNA−NP layer at the interface due to the electrostatic particle−surface (DNA−cationic lipid) attraction, which, in turn, results in a larger deviation from the solution-like morphology of the DNA corona. Interestingly, a nonmonotonic adsorption of duplex DNA chains on oppositely charged nanoparticle surface was reported at high salt concentration.[43] Our 2D nanoparticle system (S_{C50_B50}) exhibits a monotonic, weak power law dependence (Supporting Information Figure S5) at high salt (>100 mM).

The power law scaling analysis of the in-plane DNA corona thickness, H, further confirms the deviation from bulk behavior. We evaluated the dependence of H on the salt concentration using the power law form $H \sim C_s^{\gamma}$ (Figure 5). The exponent γ provides a measure of the dependence of the corona thickness on the salt concentration, where $\gamma = 0.33$ is typically observed for polyelectrolyte brushes in the bulk solutions.[44−46] The log−log plot $H(C_s)$ for the three studied systems along with the fits for γ are shown in Figure 5. Analogously with the DC model analysis discussed above, we find that deviation of γ from bulk value (~0.33) is greater for the systems with stronger interacting DNA−NP and the lipid layer. This analysis suggests that the DNA shell morphology is significantly modified at the lipid layer in comparisons to the bulk behavior.

While the detailed quantitative description of the above-discussed confinement effect calls for future theoretical efforts, here we seek a qualitative understanding of the observed differences in the $H(C_s)$ behavior for the various systems. The deviations from the bulk behavior can be understood in terms of the interplay of the morphologies of the DNA chains adsorbed at the interface and the chains on the bulk side of NP that are not adsorbed at the interface. At the charged interface, the interparticle separation is determined by both parts of the DNA corona−the part that is not adsorbed at the interface (referred to as the NP's 3D subcorona) and the DNA chains adsorbed at the interface (the NP's 2D DNA subcorona) as shown in Figure 5b. These 2D and 3D parts of the DNA coronas are affected differently by the salt concentration, and the relative contribution of each part changes depending on the interfacial charge density and the DNA length. The repulsion between the charges in the 2D subcorona is already partially screened by the presence of the cationic lipids. Thus, the 2D subcorona should be less sensitive to the salt concentration changes than the 3D subcorona.

We now examine the relative importance of the 2D and 3D subcoronas in dictating the interparticle spacing in the studied systems. For the system S_{C100_B65}, which has the largest DNA shell and the highest charge density on the lipid monolayer, and thus the strongest NP-surface interactions, the measured exponent is $\gamma \sim 0.13$, corresponding to the largest deviation from bulk value among the three systems studied. This result is consistent with our expectation that S_{C100_B65} is the system in which the effect of the 2D electrostatic confinement is the most dominant, *i.e.*, the 2D subcorona is the largest, and consequently, the dependence on salt concentration will be the weakest. For the system S_{C100_B50}, γ is about 0.20, suggesting that the contribution to the interparticle distance from the 3D subcorona increases while that from the 2D subcorona declines. Finally, for S_{C50_B50}, where the 2D confinement effect is expected be the smallest among the three systems, the power law exponent ($\gamma \approx 0.26$) approaches the value, 0.33, for polyelectrolyte brushes in bulk solution, suggesting the predominant contribution of the 3D subcorona. The analysis suggests that in the 2D system of DNA−NPs that are electrostatically bound to the lipid layer, the competing effects of the 2D and 3D DNA subcoronas determine the behavior of nanoparticle packing with ionic strength. This result has important implications for a variety of interfacial systems where NPs with charged soft shells interact with charged interface.

On the basis of the discussed relative contributions of the 2D and 3D subcoronas, we can explain the observed crossover behavior of d and ρ between C_s = 0 and 5 mM (Figure 4). Our interpretation of this behavior is summarized schematically on Figure 5b. At zero salt, where the DNA chains are almost completely stretched out and 3D corona dominates, the interparticle distance is larger for S_{C50_B50} than for S_{C100_B50} because a smaller fraction of chains are adsorbed at the interface as result lower density of lipid charges for S_{C50_B50}. With the addition of salt, the shrinkage of the 3D subcorona leads to the dominance of 2D subcorona in defining the interparticle distances. The 2D subcorona is larger for the system S_{C100_B50}, which has a

higher density of lipid charge than for S_{C50_B50}; hence, this results in the observed crossover behavior.

CONCLUSION

We have demonstrated the formation of ordered and salt-tunable 2D nanoparticle arrays at the lipid-coated air−water interface. The particle−particle and particle−surface interactions were controlled by changing the salt concentration. The influence of the system design parameters, such as the length of DNA chains in the NP shell and the charge density of the lipid layer, was investigated. The NP density in the monolayer can be tuned by up to ∼4 times *via* ionic strength with controllable changes of the in-plane interparticle spacing, as was investigated by the *in situ* studies using surface X-ray scattering methods (GISAXS and XRR). The major mechanism for the observed tunability of the arrays is related to the decrease of the DNA persistence length with salt increase, which results in the reduction of interparticle distances. Consequently, the adsorption of additional nanoparticles to the lipid interface occurs due to the newly available area; thus, NP monolayer density is increased with salt concentration.

Our analysis based on the Daoud−Cotton model and power law scaling for salt-dependent behavior of bulk polyelectrolyte systems reveals that 2D assembly exhibits a peculiar dependence on a salt concentration, different from bulk systems. The comparison with predictions for bulk polyelectrolyte systems suggests that the deviations for the studied DNA-coated NPs at the charged interfaces arise from the deformation of DNA shells. We attribute this deformation to the nanoparticle confinement at the lipid interface through electrostatic nonuniform interactions of the NP shell with the charged lipid layer. The confinement results in the interplay of 2D and 3D effects, which determine the interparticle distances within the 2D NP array. Our findings on the behavior of nanoparticle soft shell at the charge interface are of importance for a broad range of nanoscale interfacial systems, and the detailed theoretical studies are called for to fully understand the observed phenomena.

MATERIALS AND METHODS

The charged interfaces were prepared by depositing the monolayer of neutral and cationic lipid at water surface by using the Langmuir method. The neutral 1, 2-dimyristoyl-*sn*-glycero-3-phosphocholine (DMPC) and cationic lipids, 1, 2-dimyristoyl-3-trimethylammonium-propane (DMTAP) were purchased from Avanti Polar Lipids, Inc. Lipid membranes with different positive charge density of the cationic lipid, DMTAP, were prepared by mixing desired composition of neutral and cationic lipid in chloroform solution at appropriate molar ratio. The NPs were purchased from Ted Pella and sizes of the nanoparticles from SAXS measurement were estimated as 8.5 (±0.75) nm (Supporting Information Figure S1). Gold nanoparticles were functionalized with noncomplementary thiolated ssDNA chains (Integrated DNA technologies) of varying length, 50 and 65 bases. All other chemicals used in this study were purchased from Sigma-Aldrich. Ultrapure water (Millipore, 18.2 MΩ cm) was used throughout sample preparation. The home-built Teflon troughs with fixed area of 2535 mm^2 were used in the experiments.[15,17] The trough was equipped with a Delrin port for injection of the gold nanoparticle solution into subphase without disturbing the lipid membrane. The trough held 9 mL of subphase (water) in volume. The trough was enclosed in an aluminum box filled with humidified helium which helped to reduce the background scattering and radiation-induced oxidation. For in-plane study, the flight path for the detector was continuously flowed with helium gas for higher signal-to-noise ratio. The measurements were done at constant temperature of 25 °C which was controlled by circulating water at constant temperature through the aluminum plate underneath the trough. In a typical experiment, ∼60 μL of 0.1 mM of lipid solution in chloroform was spread on the thoroughly cleaned water surface using Hamilton syringes to form monolayer of lipid with average molecular area of ∼75 $Å^2$/lipid. The surface pressure at the air/water interface, measured using a precalibrated paper Wilhelmy plate, varied between 8 and 14 mN/m. After equilibration time of 20−30 min, 500 μL (∼200 nM) of nanoparticle solution in water functionalized with noncomplementary ssDNA chains was added to the subphase. Upon adding the NPs, 2D assembly was instantaneously observed. A schematic of the experimental setup is described in Figure 1. However, for studying the structure of 2D assemblies at different ionic strength, a sample was allowed to equilibrate for at least 8−10 h after adding the salt.

The *in situ* Grazing Incidence Small Angle X-ray Scattering (GISAXS) and X-ray reflectivity (XRR) measurements were performed to study the structure formation and their development simultaneously both in plane and normal to the Langmuir monolayer. The *in situ* GISAXS and XRR were carried out at Beamline X22B of the National Synchrotron Light Source (NSLS). The critical angle for water at incident energy 8.2 Kev is 0.15°. In our experiments, incident angle, α, was fixed at 0.2° to ensure that the X-rays penetrate the entire depth of the nanoparticle layer. The schematic of the scattering geometry is shown in Figure 1c. The scattering vector **q** was calibrated by measuring the scattering pattern from a silver behenate standard sample. The wave vectors $k_i = k_o = 2\Pi/\lambda$, where the x-ray energy was kept fixed at λ = 1.517 Å. The perpendicular and in-plane components of scattering vector are defined as $q_z = k_o (\sin \alpha_i + \sin \alpha_f)$, $q_y = k_o (\cos \alpha_f \sin \theta)$ and $q_x = k_o (\cos \alpha_f \cos \theta - \cos \alpha_i)$ where angles are as defined in Figure 1c. Exposure time of 100 s with incident flux of $\sim 10^8$ ph/s was used for recording the GISAXS images from the different region of the sample. No damage of the samples was observed at this exposure time. In XRR, the outgoing angle is equal to the incident angle ($\alpha_f = \alpha_i = \alpha$) and $\theta = 0$. The specularly reflected intensity from the surface is measured as a function of the incident angle α or wave vector transfer $q_z = (4\Pi/\lambda) \sin \alpha$. The protocol for the XRR measurement was optimized for different q_z ranges to minimize x-ray induced structural changes in the monolayer of lipid bound NPs.

Conflict of Interest: The authors declare no competing financial interest.

Acknowledgment. Research carried out at the Center for Functional Nanomaterials, Brookhaven National Laboratory, which is supported by the U.S. Department of Energy, Office of Basic Energy Sciences, under Contract No. DE-AC02-98CH10886. M.F. acknowledges support by the U.S. Department of Energy, Office of Basic Energy Sciences, Division of Materials Sciences and Engineering, under Contract No. DE-AC02-98CH10886. Use of the National Synchrotron Light Source was supported by the U.S. Department of Energy, Office of Basic Energy Sciences, under Contract No. DE-AC02-98CH10886.

Supporting Information Available: Additional experimental details and GISAXS data. This material is available free of charge *via* the Internet at http://pubs.acs.org.

REFERENCES AND NOTES

1. Yella, A.; Lee, H. W.; Tsao, H. N.; Yi, C. Y.; Chandiran, A. K.; Nazeeruddin, M. K.; Diau, E. W. G.; Yeh, C. Y.; Zakeeruddin, S. M.; Gratzel, M. Porphyrin-Sensitized Solar Cells with Cobalt (II/III)-Based Redox Electrolyte Exceed 12% Efficiency. *Science* **2011**, *334*, 629–634.
2. Feldt, S. M.; Gibson, E. A.; Gabrielsson, E.; Sun, L.; Boschloo, G.; Hagfeldt, A. Design of Organic Dyes and Cobalt Polypyridine Redox Mediators for High-Efficiency Dye-Sensitized Solar Cells. *J. Am. Chem. Soc.* **2010**, *132*, 16714–16724.
3. Zhang, C.; Macfarlane, R. J.; Young, K. L.; Choi, C. H. J.; Hao, L.; Evelyn, A.; Liu, G.; Zhou, X.; Mirkin, C. A. A General Approach to DNA-Programmable Atom Equivalents. *Nat. Mater.* **2013**, *12*, 741–746.
4. Vlasov, Y. A.; Bo, X. Z.; Sturm, J. C.; Norris, D. J. On-Chip Natural Assembly of Silicon Photonic Bandgap Crystals. *Nature* **2001**, *414*, 289–293.
5. Wong, S.; Kitaev, V.; Ozin, G. A. Colloidal Crystal Films: Advances in Universality and Perfection. *J. Am. Chem. Soc.* **2003**, *125*, 15589–15598.
6. Zhu, Z. N.; Meng, H. F.; Liu, W. J.; Liu, X. F.; Gong, J. X.; Qiu, X. H.; Jiang, L.; Wang, D.; Tang, Z. Y. Superstructures and Sers Properties of Gold Nanocrystals with Different Shapes. *Angew. Chem. Int. Ed.* **2011**, *50*, 1593–1596.
7. Khizroev, S.; Hijazi, Y.; Amos, N.; Chomko, R. Physics Considerations in the Design of Three-Dimensional and Multilevel Magnetic Recording. *J. Appl. Phys.* **2006**, *100*.
8. Back, C. H.; Weller, D.; Heidmann, J.; Mauri, D.; Guarisco, D.; Garwin, E. L.; Siegmann, H. C. Magnetization Reversal in Ultrashort Magnetic Field Pulses. *Phys. Rev. Lett.* **1998**, *81*, 3251–3254.
9. Koo, J.; Shin, K.; Seo, Y. S.; Koga, T.; Park, S.; Satija, S.; Chen, X.; Yoon, K.; Hsiao, B. S.; Sokolov, J. C.; *et al.* Stabilizing, Thin Film Polymer Bilayers against Dewetting Using Multiwalled Carbon Nanotubes. *Macromolecules* **2007**, *40*, 9510–9516.
10. Moerz, S. T.; Huber, P. Protein Adsorption into Mesopores: A Combination of Electrostatic Interaction, Counterion Release, and van der Waals Forces. *Langmuir* **2014**, *30*, 2729–2737.
11. Bandyopadhyay, D.; Douglas, J. F.; Karim, A. Influence of C-60 Nanoparticles on the Stability and Morphology of Miscible Polymer Blend Films. *Macromolecules* **2011**, *44*, 8136–8142.
12. Rudiuk, S.; Yoshikawa, K.; Baigl, D. Enhancement of DNA Compaction by Negatively Charged Nanoparticles: Effect of Nanoparticle Size and Surfactant Chain Length. *J. Colloid Interface Sci.* **2012**, *368*, 372–377.
13. Kim, J. H.; Song, A. Y.; Kwon, D. H.; An, H. H.; Ahnn, H. S.; Kim, Y. K.; Yoon, C. S. Phospholipid-Driven Long-Range Ordering of Fe_3O_4 Nanoparticles. *Appl. Surf. Sci.* **2011**, *257*, 3128–3134.
14. Bigioni, T. P.; Lin, X. M.; Nguyen, T. T.; Corwin, E. I.; Witten, T. A.; Jaeger, H. M. Kinetically Driven Self Assembly of Highly Ordered Nanoparticle Monolayers. *Nat. Mater.* **2006**, *5*, 265–270.
15. Kewalramani, S.; Wang, S. T.; Lin, Y. A.; Huong, G. N.; Wang, Q. A.; Fukuto, M.; Yang, L. Systematic Approach to Electrostatically Induced 2D Crystallization of Nanoparticles at Liquid Interfaces. *Soft Matter* **2011**, *7*, 939–945.
16. Harries, D.; May, S.; Ben-Shaul, A. Counterion Release in Membrane-Biopolymer Interactions. *Soft Matter* **2013**, *9*, 9268–9284.
17. Fukuto, M.; Wang, S. T.; Lohr, M. A.; Kewalramani, S.; Yang, L. Effects of Surface Ligand Density on Lipid-Monolayer-Mediated 2D Assembly of Proteins. *Soft Matter* **2010**, *6*, 1513–1519.
18. Fukuto, M.; Nguyen, Q. L.; Vasilyev, O.; Mank, N.; Washington-Hughes, C. L.; Kuzmenko, I.; Checco, A.; Mao, Y. M.; Wang, Q.; Yang, L. Crystallization, Structural Diversity and Anisotropy Effects in 2D Arrays of Icosahedral Viruses. *Soft Matter* **2013**, *9*, 9633–9642.
19. Jiang, Z.; Lin, X. M.; Sprung, M.; Narayanan, S.; Wang, J. Capturing the Crystalline Phase of Two-Dimensional Nanocrystal Superlattices in Action. *Nano Lett.* **2010**, *10*, 799–803.
20. Li, S.; Malmstadt, N. Deformation and Poration of Lipid Bilayer Membranes by Cationic Nanoparticles. *Soft Matter* **2013**, *9*, 4969–4976.
21. Dif, A.; Henry, E.; Artzner, F.; Baudy-Floc'h, M.; Schmutz, M.; Dahan, M.; Marchi-Artzner, V. Interaction between Water-Soluble Peptidic Cdse/Zns Nanocrystals and Membranes: Formation of Hybrid Vesicles and Condensed Lamellar Phases. *J. Am. Chem. Soc.* **2008**, *130*, 8289–8296.
22. Ivankin, A.; Kuzmenko, I.; Gidalevitz, D. Cholesterol-Phospholipid Interactions: New Insights from Surface X-ray Scattering Data. *Phys. Rev. Lett.* **2010**, *104*, No. 108101.
23. Torchilin, V. P. Recent Advances with Liposomes as Pharmaceutical Carriers. *Nat. Rev. Drug Discov* **2005**, *4*, 145–160.
24. De Jong, W. H.; Borm, P. J. A. Drug Delivery and Nanoparticles: Applications and Hazards. *Int. J. Nanomed.* **2008**, *3*, 133–149.
25. Zhang, L.; Gu, F. X.; Chan, J. M.; Wang, A. Z.; Langer, R. S.; Farokhzad, O. C. Nanoparticles in Medicine: Therapeutic Applications and Developments. *Clin. Pharmacol. Ther.* **2008**, *83*, 761–769.
26. Sun, C.; Lee, J. S. H.; Zhang, M. Q. Magnetic Nanoparticles in Mr Imaging and Drug Delivery. *Adv. Drug Delivery Rev.* **2008**, *60*, 1252–1265.
27. Rosi, N. L.; Giljohann, D. A.; Thaxton, C. S.; Lytton-Jean, A. K. R.; Han, M. S.; Mirkin, C. A. Oligonucleotide-Modified Gold Nanoparticles for Intracellular Gene Regulation. *Science* **2006**, *312*, 1027–1030.
28. Kim, J. H.; Jang, H. H.; Ryou, S. M.; Kim, S.; Bae, J.; Lee, K.; Han, M. S. A Functionalized Gold Nanoparticles-Assisted Universal Carrier for Antisense DNA. *Chem. Commun.* **2010**, *46*, 4151–4153.
29. Chen, H.; Meisburger, S. P.; Pabit, S. A.; Sutton, J. L.; Webb, W. W.; Pollack, L. Ionic Strength-Dependent Persistence Lengths of Single-Stranded Rna and DNA. *Proc. Natl. Acad. Sci. U.S.A.* **2012**, *109*, 799–804.
30. Warren, B. E. *X-Ray Diffraction*. Dover ed.; Dover Publications: New York, 1990; p vii, 381 p.
31. Parratt, L. G. Surface Studies of Solids by Total Reflection of X-rays. *Phys. Rev.* **1954**, *95*, 359.
32. Nelson, A. Co-Refinement of Multiple-Contrast Neutron/X-ray Reflectivity Data Using Motofit. *J. Appl. Crystallogr.* **2006**, *39*, 273–276.
33. Yang, L.; Wang, S. T.; Fukuto, M.; Checco, A.; Niu, Z. W.; Wang, Q. Structure and Interaction in 2D Assemblies of Tobacco Mosaic Viruses. *Soft Matter* **2009**, *5*, 4951–4961.
34. Campolongo, M. J.; Tan, S. J.; Smilgies, D. M.; Zhao, M.; Chen, Y.; Xhangolli, I.; Cheng, W. L.; Luo, D. Crystalline Gibbs Monolayers of DNA-Capped Nanoparticles at the Air-Liquid Interface. *ACS Nano* **2011**, *5*, 7978–7985.
35. Fukuto, M.; Heilmann, R. K.; Pershan, P. S.; Badia, A.; Lennox, R. B. Monolayer/Bilayer Transition in Langmuir Films of Derivatized Gold Nanoparticles at the Gas/Water Interface: An X-ray Scattering Study. *J. Chem. Phys.* **2004**, *120*, 3446–3459.
36. Bera, M. K.; Sanyal, M. K.; Pal, S.; Daillant, J.; Datta, A.; Kulkarni, G. U.; Luzet, D.; Konovalov, O. Reversible Buckling in Monolayer of Gold Nanoparticles on Water Surface. *Europhys. Lett.* **2007**, *78*.
37. Schultz, D. G.; Lin, X. M.; Li, D. X.; Gebhardt, J.; Meron, M.; Viccaro, P. J.; Lin, B. H. Structure, Wrinkling, and Reversibility of Langmuir Monolayers of Gold Nanoparticles. *J. Phys. Chem. B* **2006**, *110*, 24522–24529.
38. Pieranski, P. Two-Dimensional Interfacial Colloidal Crystals. *Phys. Rev. Lett.* **1980**, *45*, 569–572.
39. Daoud, M.; Cotton, J. P. Star Shaped Polymers—A Model for the Conformation and Its Concentration-Dependence. *J. Phys. (Paris)* **1982**, *43*, 531–538.

40. Hariharan, R.; Biver, C.; Mays, J.; Russel, W. B. Ionic Strength and Curvature Effects in Flat and Highly Curved Polyelectrolyte Brushes. *Macromolecules* **1998**, *31*, 7506–7513.
41. Xiong, H. M.; van der Lelie, D.; Gang, O. Phase Behavior of Nanoparticles Assembled by DNA Linkers. *Phys. Rev. Lett.* **2009**, *102*, No. 015504.
42. Tan, S. J.; Kahn, J. S.; Derrien, T. L.; Campolongo, M. J.; Zhao, M.; Smilgies, D. M.; Luo, D. Crystallization of DNA-Capped Gold Nanoparticles in High-Concentration, Divalent Salt Environments. *Angew. Chem.* **2014**, *53*, 1316–1319.
43. Zinchenko, A. A.; Yoshikawa, K.; Baigl, D. Compaction of Single-Chain DNA by Histone-Inspired Nanoparticles. *Phys. Rev. Lett.* **2005**, *95*, 228101.
44. Hariharan, R.; Biver, C.; Russel, W. B. Ionic Strength Effects in Polyelectrolyte Brushes: The Counterion Correction. *Macromolecules* **1998**, *31*, 7514–7518.
45. Pincus, P. Colloid Stabilization with Grafted Polyelectrolytes. *Macromolecules* **1991**, *24*, 2912–2919.
46. Zhulina, E. B.; Borisov, O. V.; Birshtein, T. M. Structure of Grafted Polyelectrolyte Layer. *J. Phys. II* **1992**, *2*, 63–74.